Monthly Notices
of the
ROYAL ASTRONOMICAL SOCIETY

MNRAS **516,** 1584–1600 (2022)
Advance Access publication 2022 August 16

https://doi.org/10.1093/mnras/stac2211

Polarimetry and photometry of gamma-ray bursts afterglows with RINGO3

M. Shrestha [1]★ I. A. Steele,[1] S. Kobayashi,[1] R. J. Smith,[1] C. Guidorzi [2,3,4] N. Jordana-Mitjans [5] H. Jermak,[1] D. Arnold,[1] C. G. Mundell [5] and A. Gomboc[6]

[1]*Astrophysics Research Institute, Liverpool John Moores University, Liverpool Science Park, 146 Brownlow Hill, UK Liverpool L3 5RF, UK*
[2]*Department of Physics and Earth Science, University of Ferrara, via Saragat 1, I-44122 Ferrara, Italy*
[3]*INFN – Sezione di Ferrara, via Saragat 1, I-44122 Ferrara, Italy*
[4]*INAF – Osservatorio di Astrofisica e Scienza dello Spazio di Bologna, Via Piero Gobetti 101, I-40129 Bologna, Italy*
[5]*Department of Physics, University of Bath, Claverton Down, Bath BA2 7AY, UK*
[6]*Center for Astrophysics and Cosmology, University of Nova Gorica, Vipavska 13, 5000 Nova Gorica, Slovenia*

Accepted 2022 July 29. Received 2022 July 28; in original form 2022 April 21

ABSTRACT

We present photometric and polarimetric measurements of gamma-ray burst (GRB) optical afterglows observed by the RINGO3 imaging polarimeter over its ∼7 yr lifetime mounted on the Liverpool Telescope. During this time, RINGO3 responded to 67 GRB alerts. Of these, 28 had optical afterglows and a further ten were sufficiently bright for photometric and polarimetric analysis ($R \lessapprox 17$). We present high quality multicolour light curves of ten sources: GRB 130606A, GRB 130610A, GRB 130612A, GRB 140430A, GRB 141220A, GRB 151215A, GRB 180325A, GRB 180618A, GRB 190114C, and GRB 191016A and polarimetry for seven of these (excluding GRB 130606A, GRB 130610A, and GRB 130612A, which were observed before the polarimetry mode was fully commissioned). Eight of these ten GRBs are classical long GRBs, one sits at the short-long duration interface with a $T_{90} \sim 4$ s and one is a classical short, hard burst with extended emission. We detect polarization for GRB 190114C and GRB 191016A. While detailed analyses of several of these GRBs have been published previously, here we present a uniform re-reduction and analysis of the whole sample and investigation of the population in a broad context relative to the current literature. We use survival analysis to fully include the polarization upper limits in comparison with other GRB properties, such as temporal decay rate, isotropic energy, and redshift. We find no clear correlation between polarization properties and wider sample properties and conclude that larger samples of early time polarimetry of GRB afterglows are required to fully understand GRB magnetic fields.

Key words: magnetic fields – techniques: photometric – techniques: polarimetric – gamma-ray bursts.

1 INTRODUCTION

Gamma-ray bursts (GRBs) are extremely energetic transients occurring at cosmological distances. They have been observed at various wavelengths ranging from gamma-rays to radio and these observations help us to piece together the puzzle of GRB physics. One of the proposed scenarios is that accretion on to a compact object powers the relativistic outflow and other prediction is the magnetar spindown as the powering source for the GRB (Metzger et al. 2011). Internal dissipation in the outflow causes the prompt gamma-rays, and external shocks (interaction of the jet with local ambient medium) produce afterglow emission at various frequencies ranging from X-ray to radio (Piran 1999; Zhang & Mészáros 2004).

One of the most puzzling aspects of GRBs is the magnetic field properties of their jets which can shed light on the driving mechanism of the explosion (Lazzati 2006; Toma 2013; Covino & Gotz 2016; Kobayashi 2019). Since GRBs are cosmological in nature, we cannot obtain the spatial resolution to understand the magnetic field strength and structure of the jets with most observational methods. Photometric observations of the forward and reverse shock afterglows can constrain the relative strength of the magnetic fields in the two shock regions, whereas polarimetry can provide information about the structure of the magnetic field in the original ejecta from the GRB central engine. Thus, polarization studies of early afterglows (few minutes after the burst) are an important technique to better understand the magnetic field properties of GRB jets.

Most polarimetric studies have focused on the observation of polarization near the jet break to understand the jet opening angle (Ghisellini & Lazzati 1999; Sari 1999; Rossi et al. 2004). These jet breaks occur ∼ 1 d after the burst, at times when we observe mostly the forward shock emission which is not highly polarized (Kopač et al. 2015; Steele et al. 2017; Jordana-Mitjans et al. 2020). Increased availability of robotic telescopes and instruments designed to observe polarization of transients have facilitated the observation of earlier time signals of these GRBs (Steele et al. 2004) (minutes to hours after the burst). The early afterglow includes the signatures of reverse shocks and the magnetic field structure of the jet itself; these

★ E-mail: ms1228@truman.edu

reverse shock afterglows have higher levels of polarization compared to forward shocks (Steele et al. 2009; Mundell et al. 2013; Steele et al. 2017; Shrestha et al. 2022). These data can be utilized with current theoretical models to narrow down the physics of GRB jets.

The Liverpool telescope (LT) which is a 2.0 m fully autonomous robotic telescope at Observatorio del Roque de los Muchachos, La Palma (Steele et al. 2004). LT is equipped with polarimeters designed for rapid observations. RINGO (2006–2009), RINGO2 (2010–2012), and RINGO3 (2013–2020) are a series of polarimeters that used a rapidly rotating polaroid analyser (Jermak et al. 2016; Arnold 2017) to observe rapidly fading sources with high accuracy. RINGO and RINGO2 observed very high polarization signals of early-time optical polarization in some GRBs (Steele et al. 2009; Mundell et al. 2013). All the RINGO2 GRB observations are presented in Steele et al. (2017). In this paper, we present a unified analysis of all of the GRBs observed by final generation of the RINGO polarimeters, RINGO3. This increases the sample size of polarization data which will help us better understand the magnetic properties of GRB jets.

In this paper, we present the results of the complete set of GRBs observed by RINGO3. We present photometric analysis of ten GRBs and polarimetric analysis of seven GRBs. The paper is arranged as follows; in Section 2, we present the design of RINGO3 and different observations performed during its run time. We describe the data reduction process in Section 3 and present the polarimetric and photometric results in Section 4. We discuss the implications of these observations in Section 5. Finally, we provide concluding remarks in Section 6.

2 INSTRUMENT AND OBSERVATIONS

In this paper, we present observational data from three different instruments: RINGO3 (polarimeter), IO:O (imager), and RATCam (imager) on board the LT. Since it is a fully robotic telescope, it is optimal for time-domain astrophysics including GRB studies (Guidorzi et al. 2006). For all the instruments, basic CCD reductions such as bias subtraction, dark subtraction, flat fielding, and World Coordinate system fitting is done via an internal common pipeline.[1]

2.1 RATCam and IO:O imaging cameras

RATCam[2] (Steele 2001) and IO:O[3] were used for photometric observations. RATCam (field of view 4.6 × 4.6 arcmin) and IO:O (10 × 10 arcmin) are optical CCD cameras equipped with $u' g' r' i' z'$ filters. In this paper, we present results from camera using the r' filter because the wavelength range of this filter is closest to the *R*-band data of RINGO3 thus we can make a better comparison to the rest of the data set.

2.2 RINGO3 polarimeter

RINGO3 (Arnold et al. 2012) was the third generation of fast-readout optical imaging polarimeters on board the LT and was observing from early 2013 to 2020 January. It had a field of view of 4 × 4 arcmin, and used a polaroid that rotated at ∼0.4 Hz. The instrument was designed using three separate electron multiplying CCDs to simultaneously observe polarized images in three different wavebands. The three wavebands have wavelength ranges of 7700–10 000 Å, 6500–7600 Å, and 3500–6400 Å. We convert these filters roughly corresponding to the standard astronomical *I*, (with $\lambda_{\rm eff} \sim 8500$ Å), *R* ($\lambda_{\rm eff} \sim 7050$ Å), and *V* ($\lambda_{\rm eff} \sim 5300$ Å) bands. Each camera obtained eight exposures per rotation which were synchronized with the phase of the polaroid's rotation. RINGO3 produced 24 CCD frames (8 per camera) every 2.3 s which were stacked per camera into 1 and 10 min blocks for each eight rotor position image. Data from these eight exposures were utilized to deduce linear Stokes vectors; explained in detail in Section 3. For 10 min stacked data, we obtain a polarization accuracy up to 2.5, 1.5, and 0.5 per cent for a 17 mag source in *I*, *R*, and *V* filters, respectively. Thus, we create a 17 mag cut off for robust polarimetric analysis.

2.3 Observations

Between 2013 and 2020, a total of 67 GRB alerts as shown in Table 1 were observed by RINGO3 and 28 of them had optical counterpart. Out of 28 GRBs with optical counterparts, two had only one data point so they were excluded from this analysis. Three observations experienced instrumental issues and had incorrect pointing. Thirteen were too faint, with an *R* magnitude greater than 17, to attempt RINGO3 photometric and polarimetric analysis. Thus, ten alerts had optical afterglows which were bright enough to perform RINGO3 photometry and polarimetry. Fig. 1 shows the observational time coverage of these GRBs in the observer's and time-dilation corrected time range, along with T_{90} which is the duration between 5 and 95 per cent of counts is measured and the Burst Alert Telescope (BAT) peak time in the observer's reference frame. Three of these afterglows were observed before 2013 December; during that time period there were problems constraining the instrumental polarization induced by the two dichroic mirrors. Thus, we can only perform photometric analysis of these GRBs. In this paper, we present polarimetric results for seven out of ten bright afterglows observed by RINGO3. The properties of GRBs analysed in this paper are presented in Table 2 which contains names of the GRBs, RA, DEC, RINGO3 observation duration, T_{90}, Galactic extinction, redshift, and related references.

Results for GRB 140430A, GRB 141220A, GRB 190114C, and GRB 191016A have already been published separately in Kopač et al. (2015), Jordana-Mitjans et al. (2021), Jordana-Mitjans et al. (2020), Shrestha et al. (2022), respectively, and a detailed analysis of GRB 180618A is submitted for publication (Jordana-Mitjans et al. 2022). In this paper, we re-analyse these bursts as well as the data on the other unpublished events in order to allow a more homogeneous analysis of the entire sample.

3 DATA REDUCTION

In this section, we present the data reduction technique used to extract counts and uncertainties in counts from eight different images; these values are used to calculate both the photometric and polarization signals.

3.1 Photometry and calibration

First we perform photometric reduction on the images and extract counts and uncertainties for the eight different images. We perform aperture photometry using the PYTHON package ASTROPY PHOTUTILS (Bradley et al. 2019). We first detect sources in the field of view (FOV) with a minimum of 15 times the standard deviation of the image signal-to-noise ratio (SNR) using DAOStarFinder. Once we identify these sources, we estimate background noise using Background2D

[1] https://telescope.livjm.ac.uk/TelInst/Pipelines/
[2] https://telescope.livjm.ac.uk/TelInst/Inst/RATCam/
[3] http://telescope.livjm.ac.uk/TelInst/Inst/IOO/

Table 1. Properties of all the triggers observed by RINGO3 in ∼ 7 yr. OT stands for optical transient. GCN stands for gamma-ray burst coordinates network which is a system that distributes the information about GRBs.

GRB	RA (°)	DEC (°)	OT	$T - T_0$ (s)	IO/RATCAM	LT GCN	Note
130216A	67.90	14.67	NO	678	YES	–	–
130328A	–	–	–	246	–	–	No GCN
130408A	134.40	−32.36	YES	517	YES	14362	Only one observation
130427A	173.13	27.69	YES	47158	YES	–	Limited number of observation
130504A	272.45	−16.31	NO	193	YES	–	Only upper limit in GCN
130606A	249.3964	29.7963	YES	2097	YES	14785	Visible only in I band
130610A	224.4203	28.2072	YES	207	YES	14843	Analysis in this paper
130612A	259.7941	16.7200	YES	178	YES	14875	Analysis in this paper
GRB:130702:1	217.308	15.774	–	–	–	-	No other information
130824	288.805	10.956	NO	2253	YES	–	Not a GRB
131004A	296.11	−2.95	YES	95	YES	15306	Too faint for RINGO3(R>17)
GRB:576238:0	–	–	–	–	–	–	
131030A	345.065	−5.36	YES	3748	YES	15406	WCS error in RINGO3 observations
140206A	145.33	66.76	YES	147	YES	15806	Issue with RINGO3 observations
GRB:592204:0	–	–	–	–	–	–	Not a GRB
INTEGRAL:GRB:6599:0	–	–	–	–	–	-	Not a GRB
GRB:596958:0	202.928	29.258	–	206	YES	–	WCS error
140430A	102.9359	23.0237	YES	123	YES	16192	Analysis in this paper
140516A	252.98	39.96	NO	3158	YES	–	–
140709A	304.66	51.22	YES	101	YES	–	Faint for RINGO3 (R>17)
141026A	44.084	26.928	Maybe	196	YES	–	Faint for RINGO3 (R>17)
141220A	195.0657	32.1464	YES	128	YES	17199	Analysis in this paper
141225A	138.77	33.79	YES	278	YES	17231	Faint for RINGO3 (R>17)
150302A	175.53	36.811	NO	169	YES	–	–
150309A	277.10	86.42	NO	210	YES	17556	–
150317A	138.98	55.46	Maybe	147	NO	–	No source in the image
150428B	292.63	4.125	NO	172	YES	–	–
GRB:650221:0	7.256	59.596	NO	310	YES	–	Not a GRB
150831B	271.03	−27.25	NO	183	YES	–	–
150908	288.80	10.94	NO	1273	YES	–	Not a GRB
151118A	57.17	65.90	NO	182	YES	–	–
151215A	93.5844	35.5159	YES	181	YES	–	Analysis in this paper
160119A	211.92	20.46	Maybe	216	YES	–	Faint for RINGO3 (R>17)
160313A	183.79	57.28	NO	208	YES	19177	–
160316A	118.92	−29.56	NO	169	YES	–	Not a GRB
160401A	89.73	26.68	NO	168	YES	19254	–
160401B	–	–	NO	798	YES	–	Same field as 160401A
160401C	–	–	NO	3592	YES	–	Same field as 160401A
GRB:702630:0	299.64	35.22	NO	247	YES	–	Not a GRB
160705B	168.10	46.69	Maybe	192	YES	19658	Faint for RINGO3 (R>17)
160714A	234.49	63.80	NO	156	NO	–	–
GRB:704327:0	272.61	72.05	NO	158	NO	–	
160821B	279.97	62.39	YES	181	YES	–	Faint for RINGO3 (R> 17)
161022A	129.00	54.34	Maybe	203	YES	20090	Faint for RINGO3 (R> 17)
161214A	190.72	6.83	YES	114	YES	20252	Faint for RINGO3 (R> 17)
INTEGRAL:GRB:7644:2	190.72	6.82	–	3534	YES	–	Same as 161214A
170208B	127.14	−9.02	YES	126	YES	–	Faint for RINGO3 (R> 17)
170604B	200.80	64.19	NO	177	YES	–	–
170728B	237.98	70.12	YES	213	YES	21375	Faint for RINGO3 (R> 17)
171003A	40.91	61.43	NO	871	YES	21961	Galactic transient
GRB:778435:0	84.08	34.44	NO	159	YES	–	Not a new GRB
171020A	39.24	15.20	YES	184	YES	22033	Faint for RINGO3 (R> 17)
GRB:782859:0	40.93	61.43	NO	934	YES	–	Not a GRB
171115A	278.38	9.12	NO	211	YES	–	–
180325A	157.4275	24.4635	YES	146	YES	22534	Analysis in this paper
180512A	201.93	21.40	NO	332	YES	22716	-
GRB:841583:0	245.06	−15.70	NO	1318	YES	–	Not a GRB
180618A	169.9410	73.8371	YES	200	YES	22792	Analysis in this paper
180704A	32.66	69.96	NO	176	YES	–	-
180720C	265.63	−26.62	NO	265	YES	22991	–
180904A	274.24	46.62	NO	224	YES	23199	–
190114C	54.5048	−26.9464	YES	201	YES	–	Analysis in this paper
190427A	280.21	40.30	NO	229	YES	–	–
190624A	144.52	46.47	–	272	YES	–	Not a new source
191011A	44.72	−27.84	YES	140	NO	–	Faint for RINGO3 (R> 17)
191016A	30.2695	24.5099	YES	533	YES	–	Analysis in this paper

function of PHOTUTILS and subtract this from the data. After the background is subtracted, we perform aperture photometry, which requires the selection of the appropriate aperture size. We use two different methods to calculate the best aperture size; (1) calculate full-width at half-maximum (FWHM) of the source, and (2) calculate counts and error in counts with respect to different aperture size for one stacked image per observation. We use 2 to 3 times FWHM of the target and the aperture that produces the best counts to counts error ratio as our aperture size to perform photometry per target. We obtain eight different counts and error in counts. Error in counts

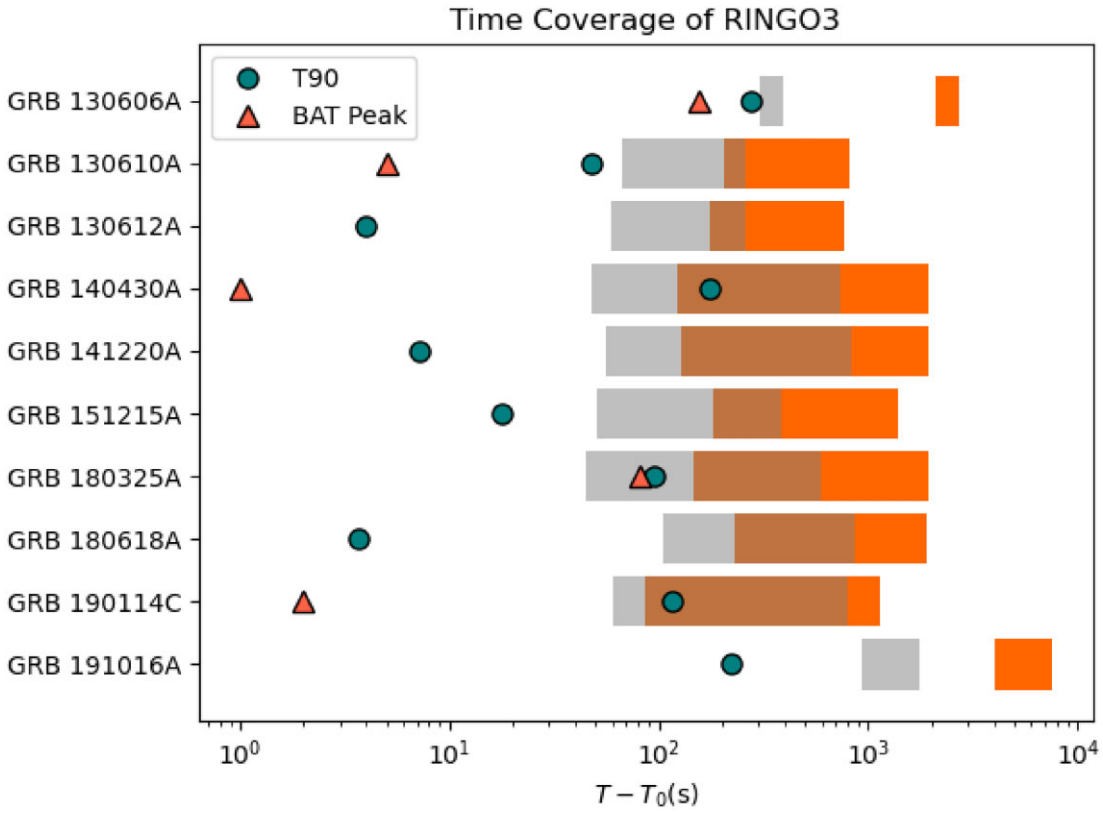

Figure 1. Plot of observation time coverage of all the GRBs analysed in this paper where the orange bar represents the observer's time range, and the grey bar represents the time-dilation corrected range. Triangular points are peak time for BAT observation in observer's frame (we do not plot BAT peak time of 0 or less) and T90 is presented as circle in observer's frame.

Table 2. Properties of the GRBs observed by RINGO3 for which we could perform photometry. Bursts from 2014 onwards could also be analysed polarimetrically. We list co-ordinates (J2000) in the second and third column, the fourth column gives MJD start time of our observations, the fifth column gives the time range observed by RINGO3, sixth is the T_{90} for the GRB and the seventh column provides the reference for these numbers, eighth column is the galactic extinction, ninth column is for jet break time ($T_{\rm JB}$), and their references is given in tenth column, redshift is given in eleventh column and their reference is provided in twelfth, and the last column gives the GCN reference of GRB detection.

GRB	RA (°)	DEC (°)	MJD start	T–T_0 (s)	T_{90} (s)	Ref.	$E(B-V)^{\rm GAL}$	$T_{\rm JB}$(d)	Ref.	z	Ref.	GCN reference
130606A	249.3964	29.7963	56449.90	2097–2697	276.6 ± 19.6	L16	0.021	>1.3	Y16	5.91	CT13	Ukwatta et al. (2013)
130610A	224.4203	28.2072	56453.13	207–807	47.7 ± 10.7	L16	0.0181	>2.9	E09	2.0920	S13	Cummings et al. (2013)
130612A	259.7941	16.7200	56455.14	176–776	4.0 ± 1.4	L16	0.065	>1.0	E09	2.0060	T13	Racusin et al. (2013)
140430A	102.9359	23.0237	56777.85	124–800	173.6 ± 3.7	L16	0.12	>1.15	K15	1.6	K14	Siegel et al. (2014)
141220A	195.0657	32.1464	57011.25	129–1929	7.2 ± 0.47	L16	0.011	>0.35	J21	1.3195	U14	Cummings et al. (2014)
151215A	93.5844	35.5159	57371.12	182–1982	17.8 ± 1.0	G15	0.34	>2.3	E09	2.59	X15	Gibson et al. (2015)
180325A	157.4275	24.4635	58202.07	147–1947	94.14 ± 1.47	T18	0.0147	>0.4	E09	2.25	He18	Troja et al. (2018)
180618A	169.9410	73.8371	58287.02	200–1400	3.71[1] ± 0.58	H18	0.058	>0.02	TW	<1.2	S18, J22	LaPorte et al. (2018)
190114C	54.5048	-26.9464	58497.87	201–2000	116.4 ± 2.56	H19	0.01	0.21	J20	0.4245	S19	Gropp et al. (2019a)
191016A	30.2695	24.5099	58772.17	3987–7587	219.70 ± 183.35	E09	0.09	0.52	S22,P22	3.29 ± 0.4[2]	S21	Gropp et al. (2019b)

Notes. References: L16 - Lien et al. (2016); G15 - Gibson et al. (2015); T18 - Troja et al. (2018); H18 - Hamburg, Bissaldi & Fermi GBM Team (2018); H19 - Hamburg et al. (2019); E09 - Evans et al. (2009); CT13 - Castro-Tirado et al. (2013); S13 - Smette et al. (2013); T13 - Tanvir et al. (2013); K14 - Kruehler et al. (2014); U14 - de Ugarte Postigo et al. (2014);X15 - Xu et al. (2015); He18 - Heintz, Fynbo & Malesani (2018);S18 - Siegel, LaPorte & Swift/UVOT Team (2018); J22 - Jordana-Mitjans et al. (2022); S19 - Selsing et al. (2019); S21 - Smith et al. (2021); Y16 - Yasuda et al. (2017); K15 - Kopač et al. (2015); J21 - Jordana-Mitjans et al. (2021); TW - This Work; J20 - Jordana-Mitjans et al. (2020); S22-Shrestha et al. (2022); P22-Pereyra et al. (2022).
1-This is a short GRB with and extended emission
2-This is photometric redshift all other are spectroscopic redshift.

are calculated via root mean square sum of background noise and Poisson noise of the source (Bradley et al. 2019).

We perform relative photometry with USNO-B1.0 (Monet et al. 2003) catalogue stars to calculate the magnitude of the GRBs. The sum of eight polarized images in a RINGO3 observations provides the total intensity of the source. For each GRB, we get simultaneous observations for three different wavebands. In the same FOV, we select one or two stars whose magnitude is already known and use those sources to calibrate the magnitude of the GRB being observed. Colour transforms from Kopač et al. (2015), Jordana-Mitjans et al. (2020) were used to convert the RINGO3 magnitudes to the standard Johnson–Cousins system. In order to correct for Galactic extinction we used Schlafly & Finkbeiner (2011) to correct the magnitude of the GRBs. To convert magnitudes to fluxes we used zeropoint values from Bessell, Castelli & Plez (1998).

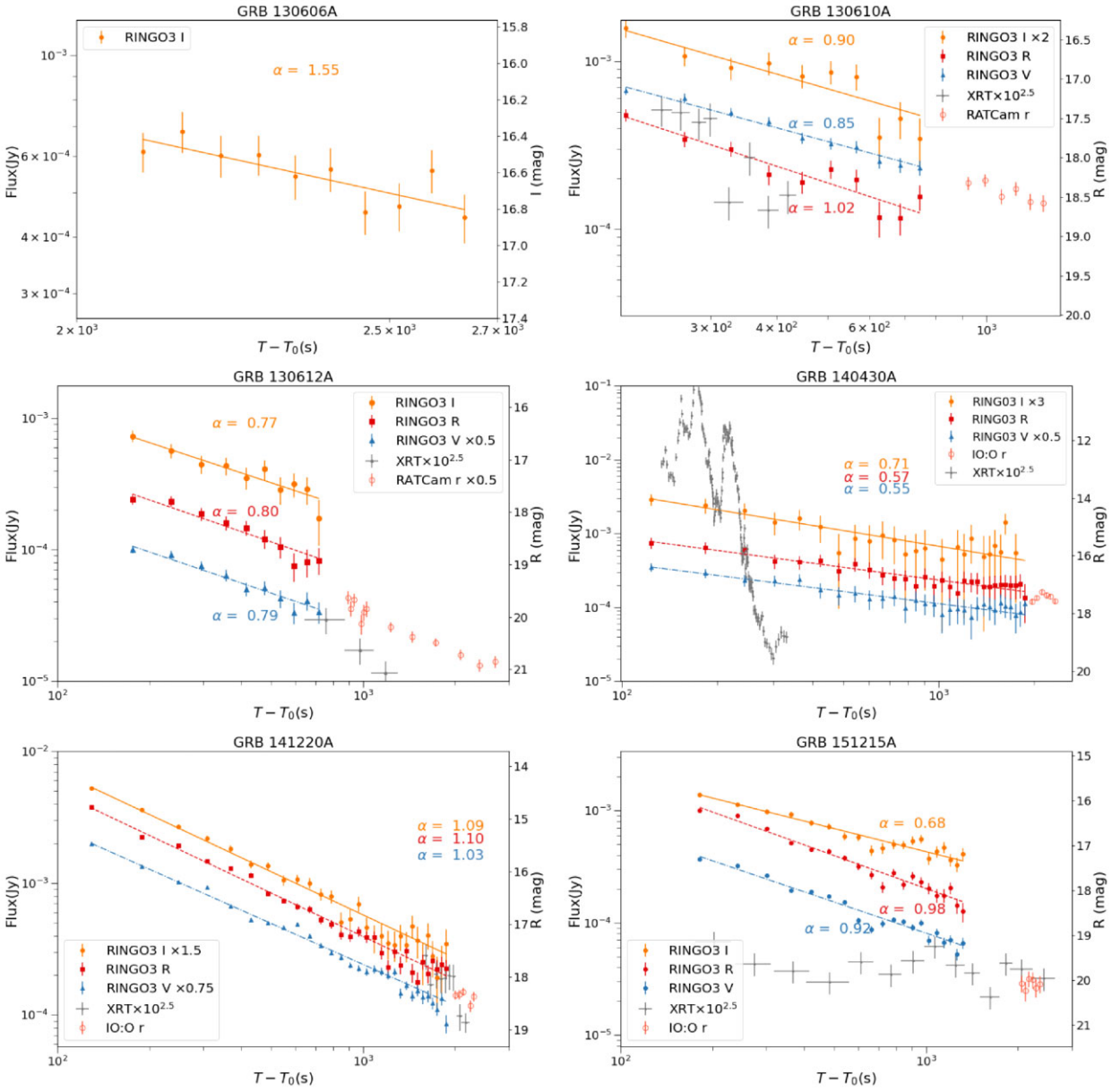

Figure 2. Light curves of the first six GRBs observed by RINGO3. Power law and broken power-law fit are performed on these GRBs according to the data observed. Power-law decay index (α) is presented in the plots for three different bands. RATCam, IO:O, and Swift XRT data are plotted as well. Left y-axis and x-axis are in log scale. For all the cases, background is estimated using 2D background estimate.

Properties such as redshift and high energy burst duration from literature for all ten GRBs are presented in Table 2. In Fig. 1 we present the time coverage of GRB observations by RINGO3 in observer frame in red and in co-moving frame in grey. The BAT peak time and T_{90} in the observer frame are presented as triangles and circles in the same plot for all ten GRBs. The light curves of all ten GRBs observed are presented in Figs 2 and 3. We fit the optical light curves of RINGO3 data with either a simple (PL) or broken power (BPL) and provide reduced χ^2 value for each fit in the Tables 3 and 4, respectively. We perform a PL or BPL fit for each waveband observation separately, thus giving us different decay indices (α) for different wavelength observations. For GRB 191016A, we perform a PL fit for IO:O data as well to see the earlier time decay index compared to later time observations made by RINGO3.

3.2 Polarization signal

The sky-subtracted counts of the eight different images are used to extract polarization of the source using recipe shown by Clarke & Neumayer (2002). The same process is followed for RINGO, RINGO2, and previous RINGO3 analysis (e.g. Jermak et al. 2016; Shrestha et al. 2022). Using this technique, we can get linear Stokes parameters q and u.

In every case we need to correct for polarization introduced by the instrument itself, therefore we observe different unpolarized and polarized standards. We take the average of Stokes q and u for the unpolarized standard star, with the assumption that the unpolarized standard star has Stokes $q \sim 0$ and $u \sim 0$, and calculate the average values introduced by the instrument. With the instrumental Stokes parameters being $q_{\rm inst}$ and $u_{\rm inst}$, the instrument corrected Stokes

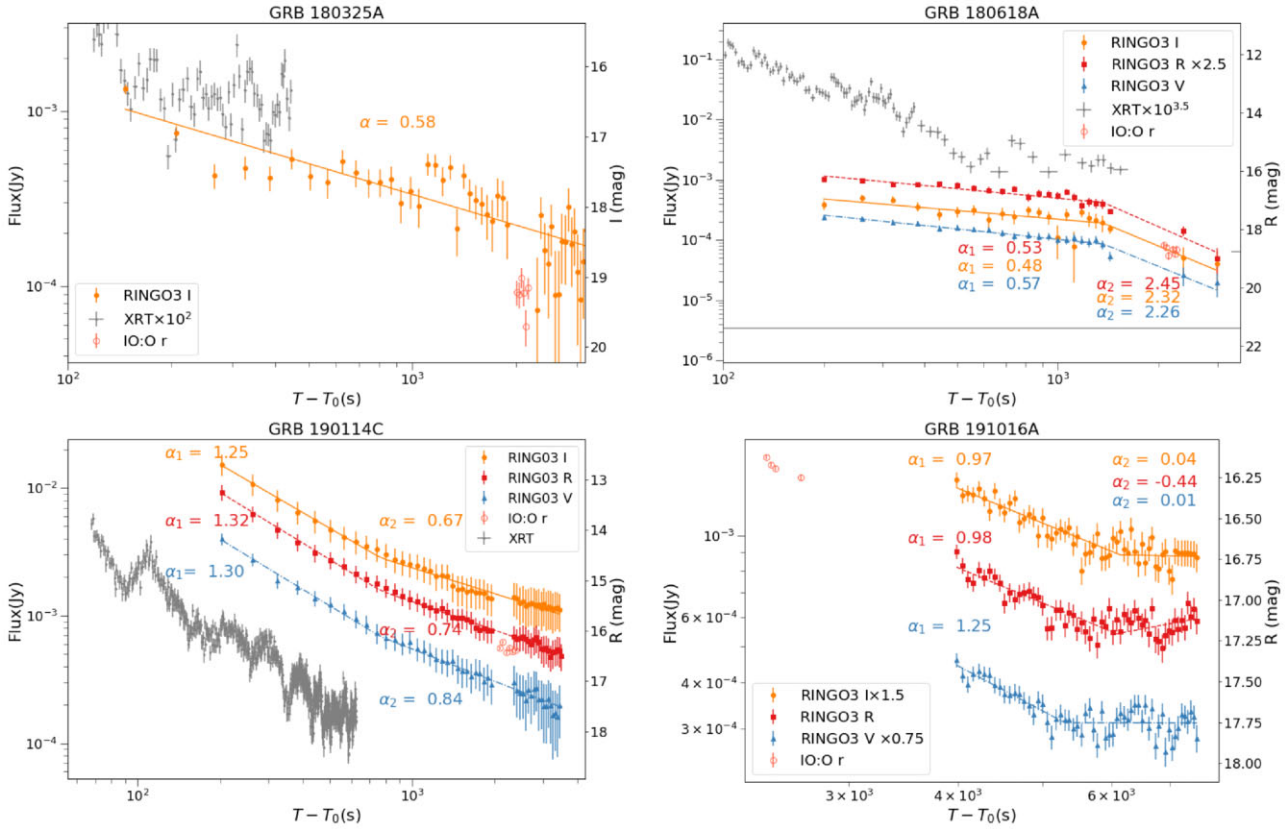

Figure 3. Light curves of the last four GRBs observed by RINGO3. Power law and broken power-law fit are performed on these GRBs according to the data observed. Power-law decay index (α) is presented in the plots for three different bands. RATCam, IO:O, and Swift XRT data are plotted as well. Left y-axis and x-axis are in log scale. For all the cases, background is estimated using 2D background estimate.

Table 3. Light-curve fitting results for GRBs that can be fitted with single power-law (PL) model. PL is given by $F \propto t^{-\alpha}$ For each fit we provide reduced χ^2_r values and degree of freedom (d.o.f).

GRB	Model	αI	αR	αV	$\chi^2_r(I)$	$\chi^2_r(R)$	$\chi^2_r(V)$	d.o.f
130606A	PL	1.55 ± 0.5	–	–	6.1	–	–	8
130610A	PL	0.90 ± 0.13	1.02 ± 0.1	0.85 ± 0.05	2.2	0.85	2.7	8
130612A	PL	0.77 ± 0.07	0.80 ± 0.07	0.79 ± 0.06	1.2	1.4	1.3	8
140430A	PL	0.71 ± 0.06	0.57 ± 0.02	0.55 ± 0.02	0.4	0.2	0.2	28
141220A	PL	1.09 ± 0.02	1.10 ± 0.02	1.03 ± 0.02	1.05	2.4	4.3	28
151215A	PL	0.68 ± 0.03	0.98 ± 0.03	0.92 ± 0.03	1.7	2.9	6.0	16
180325A	PL	0.58 ± 0.04	–	–	2.04	–	–	48

Table 4. Light-curve fitting results for GRBs whose light curve is fitted by broken power-law (BPL) model. α_1 and α_2 denotes the decay index before and after the break time, respectively. For each fit we provide reduced χ^2_r values and degree of freedom (d.o.f).

GRB	Model	T_b (m)	$\alpha_1 I$	$\alpha_2 I$	$\alpha_1 R$	$\alpha_2 R$	$\alpha_1 V$	$\alpha_2 V$	$\chi^2_r(I)$	$\chi^2_r(R)$	$\chi^2_r(V)$	d.o.f
180618A	BPL	22.8	0.48 ± 0.08	2.32 ± 0.8	0.53 ± 0.04	2.45 ± 0.4	0.57 ± 0.05	2.26 ± 0.5	1.2	1.4	0.6	18
190114C	BPL	6.7	1.43 ± 0.03	0.87 ± 0.02	1.50 ± 0.02	0.94 ± 0.01	1.47 ± 0.02	0.99 ± 0.02	0.46	0.3	0.08	45
191016A	BPL	102.4 (I), 101.4 (R), 87.5 (V)	0.97 ± 0.07	0.04 ± 0.17	0.98 ± 0.07	-0.44 ± 0.17	1.25 ± 0.1	0.01 ± 0.09	0.9	1.01	1.04	56

parameters of the target are given by:

$$q_c = q - q_{\rm inst} \quad (1)$$

$$u_c = u - u_{\rm inst}. \quad (2)$$

We perform error propagation in q and u to calculate the error value q_e and u_e. Finally, these q_c and u_c are used to calculate a raw percentage polarization and position angle by using:

$$\text{per cent}p = \sqrt{q_c^2 + u_c^2} \times 100. \quad (3)$$

$$\psi = \tfrac{1}{2} \arctan\left(\tfrac{u}{q}\right). \quad (4)$$

Table 5. Table of instrument q, u, and K factor values for different time periods of observations using RINGO3. We quote standard error ($\frac{\sigma}{\sqrt{N}}$), where N is the total number of observations as the error in instrument q and u. Standard deviation (σ) is also presented. These values are much smaller than error in Stokes q and u of GRB. Instrumental q, u, and K values are from Jermak (2017).

MJD Range	$q_{\rm in}$ (I)	σ	$u_{\rm in}$(I)	σ	K (I $^\circ$)	K (I $^\circ\sigma$)
56658–56816	-0.0119 ± 0.0005	0.003	-0.0410 ± 0.0006	0.0036	57.39	4.26
56816–57202	-0.0154 ± 0.0004	0.004	0.0295 ± 0.0015	0.014	115.15	3.75
>57202	-0.0131 ± 0.004	0.025	-0.0336 ± 0.001	0.006	125.61	4.63
MJD Range	$q_{\rm in}$ (R)	σ	$u_{\rm in}$(R)	σ	K (R°)	K ($R^\circ\sigma$)
56658–56816	-0.01163 ± 0.0004	0.0024	-0.0371 ± 0.0048	0.029	55.58	3.6
56816–57202	-0.0157 ± 0.0003	0.002	0.0333 ± 0.0014	0.013	115.95	3.25
>57202	-0.0105 ± 0.0024	0.014	-0.0356 ± 0.009	0.059	124.8	5.05
MJD Range	$q_{\rm in}$ (V)	σ	$u_{\rm in}$(V)	σ	K (V $^\circ$)	K (V$^\circ\sigma$)
56658–56816	-0.0096 ± 0.0003	0.002	-0.0177 ± 0.0003	0.002	54.93	3.94
56816–57202	-0.0077 ± 0.0002	0.0018	0.0215 ± 0.0009	0.008	115.42	2.92
>57202	-0.0047 ± 0.004	0.026	-0.022 ± 0.0058	0.035	124.90	4.89

Analysis of RINGO3 data of polarized standard shows no significant instrumental depolarization (Jermak 2017).

We take measures to get the correct quadrant for the position angle. The position angle needs to be rotated based on the telescope Cassegrain axis sky position angle (SKYPA), measured east of north which gives electron vector position angle (EVPA).

$$\mathrm{EVPA} = \psi + \mathrm{SKYPA} + K. \quad (5)$$

Here K is a calibration factor which gives the position angle offset combined of the angles between the orientation of the polarizer, the telescope focal plane, and the trigger position of the angle measuring sensor. This angle offset was calculated using polarized standards observed during various time periods and the values of K are provided in Table 5. Some parts of the analysis are taken from Jermak (2017).

The last step in the polarization calculation is bias correction and error calculation for the polarization degree and EVPA. Noise in q and u introduces a polarization signal which is not intrinsic. In order to correct for this and to calculate the error in polarization degree, we use the prescription developed by Plaszczynski et al. (2014). The error in EVPA is calculated using standard error propagation applied to equation (4).

In Figs 4 and 5, we present the evolution of polarization with time for all seven GRBs for the three different wavebands I, R, and V (top to bottom panels). We present 1σ error bars in these plots for the polarization results. When the error bars in polarization degree crosses 0 per cent, then we consider the polarization to be an upper limit and upper limit value is presented by the upper end of the error bar. When we have error bars not crossing 0 per cent, we consider it to be a possible detection.

3.3 Polarization detections

In Tables 6 and 7, we present the polarization degree measurements for all the 7 GRBs which were observed by RINGO3 and bright enough for polarimetric analysis. Table 7 identifies possible polarization detections in GRB 190114C at early times (before 2003s) and in GRB 191016A at various epochs as from consideration of their error bars as outlined above.

In order to confirm the possible polarization detections, we implemented 'permutation analysis' (described in detail in Steele et al. 2017) to rigorously investigate the probabilities of the detection by looking at the individual counts at the eight rotor positions for a source. Before doing this we correct for instrumental polarization using a bright star in the field of view as an unpolarized source and dividing the GRB source counts by the unpolarized source counts at the corresponding rotor position. These corrected counts from the eight rotor positions are shuffled into all possible ordered permutations. This procedure will destroy any coherent polarization signal encoded in the data and generates $(8 - 1)!$ (5040) permutations of the corrected counts for the GRB source. Each of these permutations will have identical noise characteristics to the original data (being generated directly from it) and are then used to calculate a polarization degree. By sorting the resulting polarization values we can then generate a rank which tells us the probability of the detected polarization degree being true (as opposed to being artificially created by the transformation of noise into polarization signal due to polarization bias). We can then check the null hypothesis; if the source is unpolarized then what is the chance of getting some polarization signal due to noise in the data? For example if the rank is greater than 0.9 it means the probability of being an unpolarized source $p = 1 -$ rank will be <0.1.

Since we have carried out a total of 79 tests over the sample, using the threshold $p < 0.05$, we could of course expect ∼4 false positives to have arisen from this testing procedure under the null hypothesis that all GRBs do not show polarization. Overall we find a total of 13 such positives in the sample. The binomial cumulative probability of such an outcome is highly significant ($p < 1.e \times 10^{-4}$) indicating that at least some of our detections (∼9) should be true polarization signals.

Further evidence of the validity of the detections can be inferred from the correspondence between individual detections made by the two techniques (error bar analysis and permutation analysis). From the error bar analysis we find 13 measurements are identified as possible detections, 9 of which have permutation analysis with $p < 0.05$. Testing against the null hypothesis of no correspondence, we find the cumulative binomial probability of this outcome is $p < 1 \times 10^{-6}$, indicating a strongly significant association. In comparison only 4 out of the 65 measurements which have only error bar upper limits show a permutation $p < 0.05$ – an outcome with a cumulative binomial $p <$ 0.41 i.e. entirely consistent with the high permutation rank values in this case being spurious due to the multitrial nature of the test. Overall we are therefore confident that the nine measurements that pass both techniques (error bars and permutation analysis) are true detections of polarization. We highlight these measurements in bold text in Table 7.

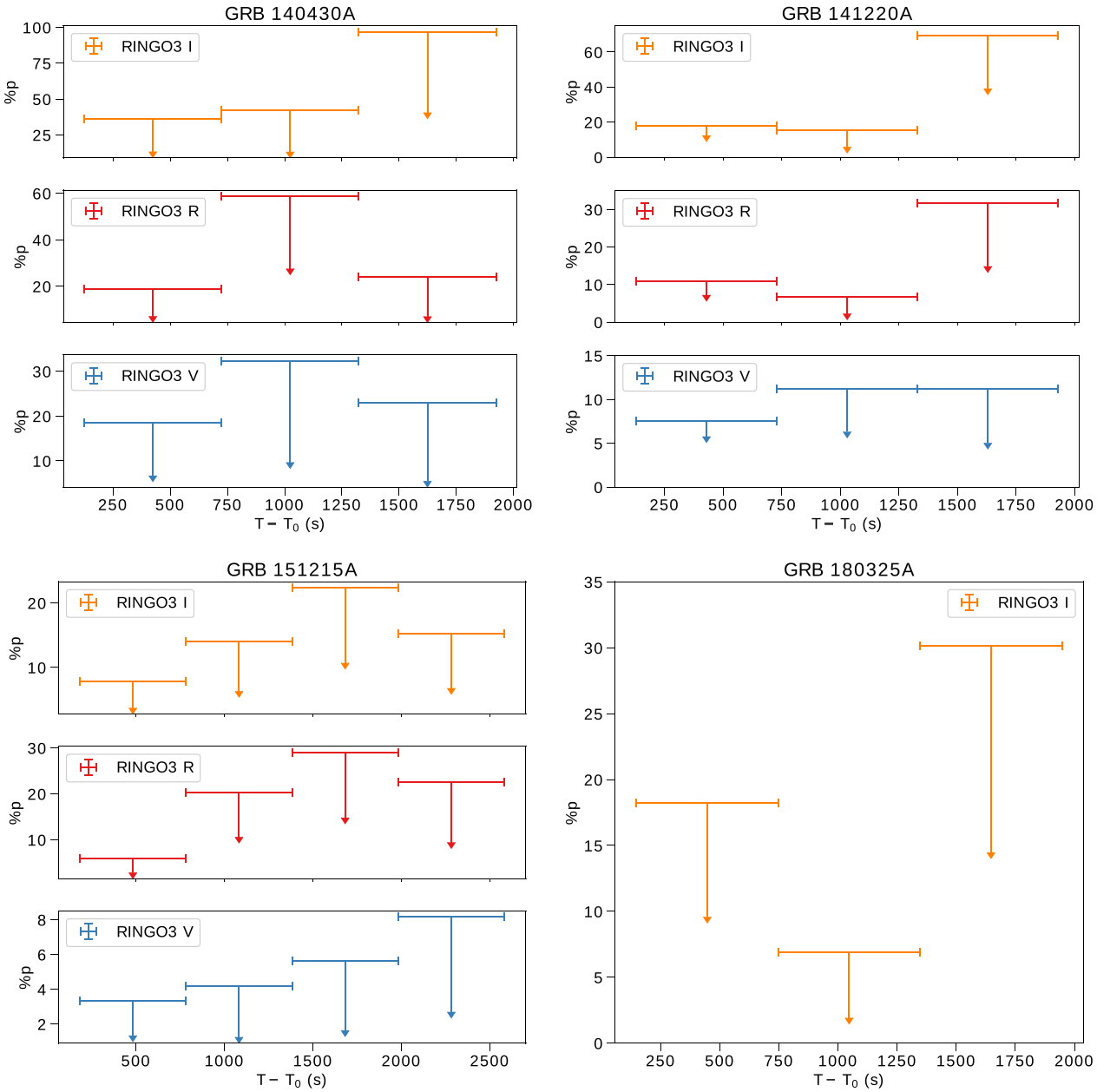

Figure 4. Observed polarization degree with respect to $T - T_0$ for the first four GRBs. For each GRB, the results in *I*, *R*, and *V* bands are presented in the top, middle, and bottom panels, respectively. Upper limits and detections are presented accordingly. Uncertainties on the x-axis are the binned exposure times for the given data point. The results presented here are not corrected for interstellar polarization.

3.4 Galactic interstellar polarization estimate

We use known GRB Milky Way Galactic extinction values to estimate the Milky way Galactic interstellar polarization (GISP) following the formulation by Serkowski et al. (1975). First we used $p^V(\mathrm{GISP}) \leq 9E_{B-V}$[4] to calculate the upper limit in polarization induced by GISP in the *V* band. For each GRB in our observed sample we used $5^\circ \times 5^\circ$ statistics from Schlafly & Finkbeiner (2011). After this calculation, we used $p/p_{\max} = \exp[-\kappa \ln^2(\lambda_{\max}/\lambda)]$ to calculate GISP in *R* and *I* bands using *V* band as the $\lambda_{\max}$ and p^V as the $p_{\max}$; where p is the polarization induced by GISP at the wavelength λ, $p_{\max}$ is the maximum polarization induced by GISP at the wavelength $\lambda_{\max}$, and κ (normally *K* is used but here to avoid confusion with *K* of EVPA constant we use κ) is a constant given to be 1.15 in Serkowski et al. (1975) and Wilking, Lebofsky & Rieke (1982) later modified it to be $\kappa = -0.10 + 1.86\lambda_{\max}$, this is used for our analysis in this paper. The GISP estimates for the seven GRBs are presented in Table 8. We do not correct for GISP in our polarization results as the GISP values are very low and can only be used for reference. We also do not correct for the ISP contribution from the host galaxy for all the GRBS. However, we present the host galactic ISP contribution for GRB 191016A and GRB 190114C, for which we have a probable detection.

[4]https://irsa.ipac.caltech.edu/cgi-bin/bgTools/nph-bgExec

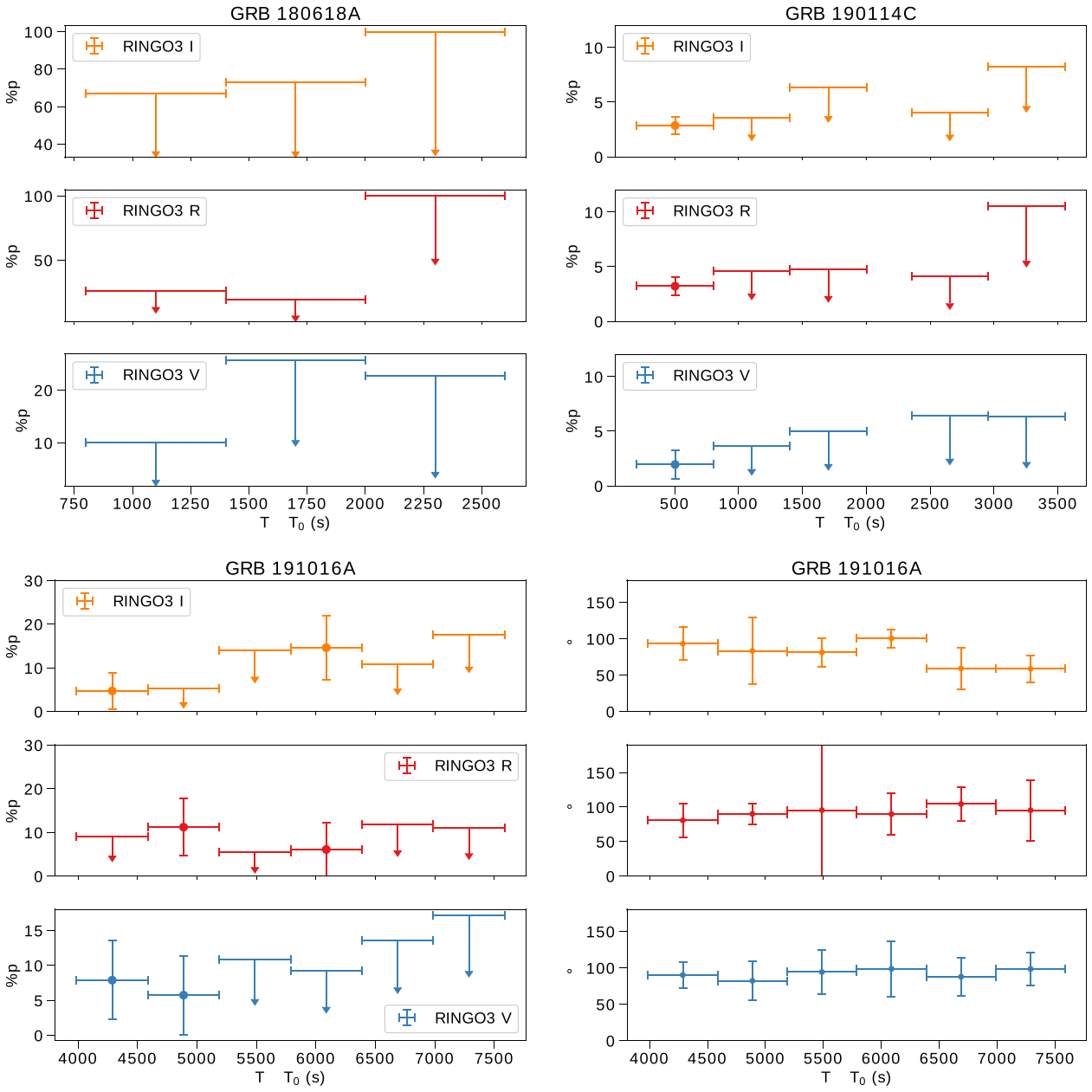

Figure 5. Observed polarization degree with respect to $T - T_0$ for the last three GRBs. For each GRB, the results in *I*, *R*, and *V* bands are presented in the top, middle, and bottom panels, respectively. Upper limits and detections are presented accordingly. Uncertainties on the x-axis are the binned exposure times for the given data point. Only for GRB 191016A, the position angle plot is presented. The results presented here are not corrected for interstellar polarization.

4 RESULTS

In this section, we present the photometric results of ten GRBs and polarimetric results of seven GRBs. In Table 9, we provide a subset of flux values for GRB 130606A and full data for all the GRBs are available in machine readable format online.

4.1 GRB 130606A

RINGO3 observations of this burst were obtained ∼35 min after the trigger time of 21:04:39 UTC (Ukwatta et al. 2013) and only the *I* band has SNR high enough to perform photometry. The gamma-ray duration is $T_{90} = 276s \pm 20$ (Lien et al. 2016) and spectroscopic redshift of $z = 5.91$ as observed by GTC (Castro-Tirado et al. 2013). We corrected for Galactic extinctions for the GRB corresponding to $A_V = 0.064$, $A_R = 0.051$, and $A_I = 0.036$. We fit a power law to the light curve and get a decay index of 1.55 ± 0.5 as shown in Fig. 2 and Table 3. *Swift* XRT data are best fitted by two breaks at 482^{+243}_{-393} s and $2.1^{+0.6}_{-0.3} \times 10^4$ s with a decay index of $0.63^{+0.09}_{-1.77}$, 1.09 ± 0.05, and $1.79^{+0.22}_{-0.19}$ (Evans et al. 2009). Yasuda et al. (2017) constraint the jet break time to be greater than 1.3 d. Polarimetric analysis are not presented here because we could not constrain the instrument polarization during this period.

Table 6. Table of polarization degree measurements from the observation done by RINGO3. The upper limit of polarization for each time interval is presented along with the upper limit for stacked data of the whole observation is presented for each GRB. The presented data are not Milky Way ISP corrected. Columns are GRB identifier, time range, polarization degree for *I*, *R*, and *V* bands, permutation rank for detected polarization.

GRB	T–T_0 (s)	P (per cent) (I)	P (per cent) (R)	P (per cent) (V)	Rank (I)	Rank (R)	Rank (V)
140430A	124–724	<35.9	<18.9	<18.50.97	0.67	0.20	–
140430A	724–1324	<42.2	<58.6	<32.3	0.78	0.68	0.66
140430A	1324–1924	<96.91	<24.1	<23.0	0.78	0.54	0.30
140430A	124–1924	<12.6	<9.6	<16.5	0.97	0.11	0.099
141220A	129–729	<17.9	<10.8	<7.5	0.88	0.67	0.79
141220A	729–1329	<15.3	<6.7	<11.1	0.45	0.69	0.21
141220A	1329–1929	<69.5	<31.7	<11.2	0.84	0.76	0.57
141220A	129–1929	<3.52	<3.23	<1.74	0.33	0.13	0.73
151215A	182–782	<7.8	<5.9	<3.3	0.31	0.199	0.065
151215A	782–1382	<14.0	<20.27	<4.2	0.16	0.73	0.051
151215A	1382–1982	<22.34	<28.9	<5.6	0.67	0.37	0.95
151215A	1982–2582	<15.2	<22.5	<8.2	0.047	0.044	0.32
151215A	182–2582	<6.45	<6.64	<6.05	0.059	0.91	0.91
180325A	147–747	<18.2	–	–	0.70	–	–
180325A	747–1347	<6.8	–	–	0.20	–	–
180325A	1347–1947	<30.1	–	–	0.24	–	–
180325A	147–1947	<12.29	–	–	0.342	–	–
180618A	800–1400	<66.0	<25.7	<10.7	0.90	0.95	0.54
180618A	1400–2000	<71.4	<19.5	<25.5	0.95	0.55	0.107
180618A	2000–2600	<100	<100	<26.0	0.88	0.78	0.53
180618A	800–2600	<5.26	<12.24	<6.78	0.38	0.61	0.078

Table 7. Table for two GRBs with polarization detection. The polarization degree for each time interval is presented and the upper limit for stacked data for the whole observation time range is also presented. The values presented are not corrected for Milky Way ISP contribution. Columns are GRB identifier, time range, polarization degree for *I*, *R*, and *V* bands, Position angle, permutation rank for detected polarization. Detections that pass both error bar and permutation analysis are highlighted in bold.

GRB	T–T_0 (s)	P (per cent) (I)	P (per cent) (R)	P (per cent) (V)	EVPA (°) (I)	EVPA (°) (R)	EVPA (°) (V)	Rank (I)	Rank (R)	Rank (V)
190114C	203–803	**2.9 ± 0.8**	**3.2 ± 0.8**	**2.0 ± 1.2**	26 ± 9	48 ± 9	25 ± 25	0.98	0.997	0.99
190114C	803–1403	2.0 ± 1.5	2.5 ± 2	<3.7	–	–	–	0.147	0.32	0.87
190114C	1403−2003	3.7 ± 2.6	<4.8	<5.0	–	–	–	0.32	0.07	0.801
190114C	2354−2954	<4.1	<3.1	<6.5	–	–	–	0.156	0.82	0.99
190114C	2954−3554	<8.2	<10.5	<6.4	–	–	–	0.87	0.81	0.98
190114C	203−2003	<2.7	<2.8	<2.22	–	–	–	0.82	0.79	0.53
191016A	3987−4587	**4.7 ± 4.1**	<9.1	**7.8 ± 5.6**	93 ± 22	–	90 ± 18	0.99	0.63	0.99
191016A	4587−5187	<5.2	**11.2 ± 6.6**	**5.7 ± 5.6**	–	90 ± 15	82 ± 26	0.59	0.99	0.98
191016A	5187−5787	<14.0	<5.5	<10.8	–	–	–	0.72	0.11	0.73
191016A	5787−6387	**14.6 ± 7.2**	**6.1 ± 6.1**	<9.2	100 ± 12	90 ± 30	–	0.99	0.95	0.74
191016A	6387−6987	<10.7	<12.0	<13.5	–	–	–	0.67	0.83	0.86
191016A	6987−7587	<17.6	<11.0	<9.2	–	–	–	0.76	0.86	0.94
191016A	3987−7587	<3.82	<5.23	<3.7	–	–	–	0.34	0.141	0.097

Table 8. Table of upper limit of Galactic interstellar polarization estimates based on extinction values from Schlafly & Finkbeiner (2011) and using Serkowski, Mathewson & Ford (1975).

GRB	$E(B-V)^{\rm GAL}$	$I-$ ISP$^{\rm GAL}$(per cent)	$R-$ ISP$^{\rm GAL}$(per cent)	$V-$ ISP$^{\rm GAL}$(per cent)
140430A	0.14	1.03	1.17	1.26
141220A	0.01	0.07	0.08	0.09
151215A	0.40	2.95	3.35	3.6
180325A	0.02	0.14	0.16	0.18
180618A	0.07	0.51	0.58	0.63
190114C	0.01	0.07	0.08	0.09
191016A	0.09	0.66	0.75	0.8

4.2 GRB 130610A

RINGO3 photometric observations were obtained in *I*, *R*, and *V* bands ∼3 min after the trigger time of 3:12:13 UTC and RATCam observations were obtained in SDSS g', r', and i' band ∼18 min after the trigger. We used stars in the field to do photometric calibrations and corrected for Galactic extinction corresponding to $A_V = 0.058$, $A_R = 0.046$, $A_I = 0.033$, $A_{g'} = 0.071$, $A_{r'} = 0.049$, and $A_{i'} = 0.037$. A simple power law is fitted to all the data in three different wave bands. We get $\alpha = 0.90 \pm 0.13$, 1.02 ± 0.1, and 0.85 ± 0.05 for *I*, *R*, and *V* filters. We note that for *R*-band images there is a dark line running through the image where the GRB is located which has been seen previously in RINGO3 R images. We found that the light-curve behaviour is dependent on how we subtract the background noise. When the median of the image is considered the background, we

Table 9. Sample photometry of GRB 130606A. Here columns are GRB name, RINGO3 Filter, T_{start} is the start time of exposure in seconds since the trigger time, T_{exp} is exposure time in seconds, F_ν is flux in mJy, and $F_\nu$err is error in flux in mJy. This table is available in its entirety in machine-readable form.

GRB	Filter	T_{start}(s)	Exp(s)	F_ν (mJy)	$F_\nu$err(mJy)
130606A	*I*	2097.0	60	0.615	0.061
130606A	*I*	2157.0	60	0.681	0.070
130606A	*I*	2217.0	60	0.603	0.063
130606A	*I*	2277.0	60	0.605	0.061
130606A	*I*	2337.0	60	0.543	0.060
130606A	*I*	2397.0	60	0.563	0.062
130606A	*I*	2457.0	60	0.453	0.050
130606A	*I*	2517.0	60	0.467	0.056
130606A	*I*	2577.0	60	0.558	0.060
130606A	*I*	2637.0	60	0.441	0.054

get the decay index to be 0.56 ± 0.05 which is much lower than the value we get when we use a 2D background estimate. We present results in this paper using 2D background estimate. *Swift* XRT and RATCam data are also presented in the Fig. 2 along with RINGO3 data and the power-law fit. This GRB has $T_{90} = 47 \pm 11$ s (Lien et al. 2016) and a spectroscopic redshift of $z = 2.092$ (Smette et al. 2013). The *Swift* XRT light curve was fitted by one break at 242^{+27}_{-33} s with a decay index of $2.47^{+0.44}_{-0.29}$ and 1.09 ± 0.03 before and after the break (Evans et al. 2009). From the *Swift* XRT light curve, we assume the minimum jet break time to be 2.9 d (Evans et al. 2009).

4.3 GRB 130612A

This is the one of the GRBs in the sample that might be argued to be a short burst ($T_{90} = 4.0 \pm 1$ s; Lien et al. 2016) and was observed around 3 min after the trigger time of 3:22:23.361 UTC as reported by *Swift*. RINGO3 photometric observations were made in *I*, *R*, and *V* bands and RATCam observations were obtained in SDSS g', r', and i' band. Calibration was done using stars in the field and the Galactic extinction correction corresponded to $A_V = 0.204$, $A_R = 0.161$, $A_I = 0.115$, $A_{g'} = 0.251$, $A_{r'} = 0.174$, and $A_{i'} = 0.129$. Fig. 2 shows the light curve of GRB 130612A for all three filters of RINGO3 including RATCam and *Swift* XRT data. Power-law fits are applied to RINGO3 data with $\alpha = 0.77 \pm 0.09$, 0.85 ± 0.09, and 0.80 ± 0.06 for *I*, *R*, and *V* filters, respectively. *Swift* XRT data were best fitted by single power law with a decay index of 1.03 ± 0.06 (Evans et al. 2009) and this gives the minimum jet break time to be 1 d. The redshift of the GRB was established spectroscopically to be $z = 2.006$ (Tanvir et al. 2013).

4.4 GRB 140430A

Kopač et al. (2015) presented polarization and photometric results for GRB 140430A. Here we performed a simple power-law fit as we did for other GRBs for consistency. For RINGO3 data, we find a decay index of $\alpha = 0.71 \pm 0.06$, 0.57 ± 0.02, and 0.55 ± 0.02 for *I*, *R* and *V* filters, respectively (Fig. 2). We note that here we are using 60 s stacked data whereas Kopač et al. (2015) used 10 s exposure data, hence there is difference in the light curve and decay index values. *Swift* XRT data were best fitted with three breaks at 320^{+17}_{-16}, 412^{+26}_{-15}, and $3.4^{+3.6}_{-1.6} \times 10^4$ s with a decay indices of $3.64^{+0.23}_{-0.19}$, $8^{+0.0}_{-1.46}$,, $0.64^{+0.06}_{-0.08}$, and $1.14^{+0.29}_{-0.23}$ (Evans et al. 2009). The minimum jet break time is assumed to be 1.15 d from Kopač et al. (2015). This burst is a relatively long burst with $T_{90} = 174 \pm 4$ and the X-ray light curve shows early flares which have been suggested to originate due to internal dissipation processes (Zhang et al. 2006; Kopač et al. 2015; Troja et al. 2015). We performed a permutation analysis on the polarimetric data and found no probable detection. For the stacked data we find polarization upper limits of < 12.6 per cent, < 9.6 per cent, and < 16.5 per cent for *I*, *R*, and *V* filters, respectively. We find a similar upper limit of polarization as Kopač et al. (2015) for all the different wavelengths. We note that our upper limit values, as stated in Table 6, are slightly different because we implement a different technique for error calculations and the time intervals of these measurements are different. The GISP estimates for this GRB are 1.03 per cent, 1.17 per cent, and 1.03 per cent for *I*, *R*, and *V* band, respectively. All the results presented in Fig. 4 are for 10 min stacked data.

4.5 GRB 141220A

RINGO3 made observations of the GRB about 3 min after the trigger time of 6:02:52 UTC in all the three USNO *I*, *R*, and *V* bands. IO:O SDSS r' band observations were made 33 min after the trigger. We used field stars to calibrate magnitude and flux. Galactic extinctions of $A_V = 0.035$, $A_R = 0.027$, $A_I = 0.02$, $A_{r'} = 0.029$ were corrected. The redshift of 1.3195 was inferred from spectroscopic observations done using OSIRIS at the 10.4 m GTC (de Ugarte Postigo et al. 2014) and gamma-ray burst duration is $T_{90} = 7 \pm 0.5$ s (Lien et al. 2016). We fit a power-law function to RINGO3 observations of GRB 141220A and get a decay index of $\alpha = 1.09 \pm 0.02$, 1.10 ± 0.02, and 1.03 ± 0.02 for *I*, *R* and *V* filters, respectively as shown in Fig. 2 and these values match well with the decay indices reported in Jordana-Mitjans et al. (2021) of 1.105 ± 0.013, 1.067 ± 0.009, and 1.095 ± 0.005 for *I*, *R*, and *V* filters. The *Swift* XRT light curve could be fitted by broken power law with a time break at 207^{+101}_{-45} s and decay index of −0.3 ± 0.6 and $1.375^{+0.104}_{-0.099}$ before and after the break (Evans et al. 2009). Jordana-Mitjans et al. (2021) reports a jet break time of 0.35 d or longer.

We present upper limit on bias-corrected polarization degree in Fig. 4 for all three wavelengths for 10 min stacked data. Jordana-Mitjans et al. (2021) found polarization detection for the first epoch in *V* band and upper limits for the rest. However, in our analysis we do not find any detection and only upper limits for all the cases. This could be due to the difference in time bin of the presented results. Though the upper limit values from this analysis does not match exactly with results from Jordana-Mitjans et al. (2021), the trend of polarization for different filters i.e. *V*, *R*, and *I* bands have an upper limit in incremental order is the same. In addition, the behaviour with time is consistent for all the filters with results from Jordana-Mitjans et al. (2021). The observed polarization degree data for the 30 min stacked data are < 3.52 per cent, < 3.23 per cent, and < 1.74 per cent for *I*, *R* and *V* bands, respectively. For this GRB, the GISP is estimated to be 0.07 per cent, 0.08 per cent, and 0.09 per cent for *I*, *R*, and *V* bands thus contribution from GISP is negligible. Since we are observing forward shock dominated emission, the low level of polarization detection is in line with theoretical predictions (Rossi et al. 2004; Kobayashi 2019).

4.6 GRB 151215A

LT observations started within 3 min of the trigger time 3:01:28 UTC. Spectroscopic analysis of NOT observations gave the redshift of $z = 2.59$ (Xu et al. 2015). The gamma-ray burst duration is $T_{90} = 18 \pm 1$ s (Gibson et al. 2015). We fit a single power law and get $\alpha = 0.68 \pm 0.03$, 0.98 ± 0.03, and 0.92 ± 0.03 for *I*, *R* and *V* filters,

respectively. In Fig. 2, the decay index is slightly different for the *I* band compared to the *R* and *V* bands. We note that there is another light source close to the target which could contaminate the GRB's aperture photometry in some cases. Thus, we cannot confirm colour evolution of the GRB. *Swift* XRT data are best fitted by a power law of decay index $0.95^{+0.06}_{-0.05}$ (Evans et al. 2009) and this data put a lower limit on the jet break time to be 2.3 d.

We present bias-corrected polarization degree values at different times for GRB 151215A in Fig. 4. We do not detect polarization and upper limit of observed polarization is presented. The polarization values for 40 min of stacked data are $<$ 6.45 per cent, $<$ 6.64 per cent, and $<$ 6.05 per cent for *I*, *R*, and *V* bands, respectively. The estimated GISP values are 2.95 per cent, 3.35 per cent, and 3.6 per cent for *I*, *R*, and *V* bands, respectively, which is a significant factor compared to the upper limit values.

4.7 GRB 180325A

RINGO3 observations started ∼13 min from the trigger time 01:53:02 and reliably detected the transient in the *I* filter only. In Fig. 3 we present the *I*-band light curve of the GRB along with limited, late-time IO:O $r^{'}$ data. We find a decay index of $\alpha = 0.58 \pm 0.04$ which is less than 1; we attribute it to the GRB forward shock for RINGO3 I data with possibility of energy injection. *Swift* constrained the gamma-ray burst duration to $T_{90} = 94 \pm 2$s (Troja et al. 2018). The redshift was obtained spectroscopically by NOT as $z = 2.25$ (Heintz et al. 2018). The *Swift* XRT best-fitting light curve has three breaks at 238^{+31}_{-116}, 2128^{+812}_{-461}, $3.5^{+0.6}_{-0.4} \times 10^4$ s with decay indices of $-0.75^{+0.22}_{-0.68}$, $0.24^{+0.27}_{-0.25}$, 1.99 ± 0.08, and 5^{+3}_{-2} (Evans et al. 2009). Using this XRT light curve, we assume a lower limit on jet break time to be 0.4 d.

The polarization degree values after bias correction are presented in Fig. 4 for *I* band. Permutation analysis on the polarization values did not show any significance for all the observed data points. For the first 30 min of stacked data we obtain $<$ 12.29 per cent for *I* band. The GISP for this case is 0.15 per cent in *I* band.

4.8 GRB 180618A

RINGO3 made observations of the GRB about 3 min after the trigger time of 0:43:13 UTC in *I*, *R*, and *V* bands. After 30 min of observations by RINGO3, IO:O was online and made follow-up observations of the GRB in SDSS *r*-band filter. Stars in the field of view were used to calibrate the magnitude and flux of the GRB and Galactic extinction of $A_V = 0.182$, $A_R = 0.144$, $A_I = 0.103$, $A_{r'} = 0.155$ correction was implemented in the results. The gamma-ray duration is $T_{90} = 3.7 \pm 0.6$ s from Fermi GBM observations and *Swift* UVOT filter detection put the upper limit on the redshift to be $z < 1.2$ (Siegel et al. 2018).

The light curve from Swift-BAT data shows a short multipeak at T_0 to $\sim T_0 + 0.3$s and extended emissions lasting until $\sim T_0 + 50$s (Sakamoto et al. 2018). They also did further analysis to get power-law index and fluence which are consistent with a short GRB with extended emission (Sakamoto et al. 2018). The Swift XRT light curve is best fitted by a power law with three breaks at 147^{+21}_{-22}, 296^{+185}_{-55}, and $5483^{+1.63\times10^3}_{-2015}$ s with decay indices of $0.80^{+0.17}_{-0.20}$, 1.48 ± 0.19, $1.876^{+0.132}_{-0.063}$, and $1.04^{+0.18}_{-0.15}$ (Evans et al. 2009).

The best fit for the RINGO3 data at all three different wavelengths is a broken power law with the same break time of 1370 s. We assume this break time to be the lower limit of jet break time as well. The best fit has $\alpha = 0.48 \pm 0.08$, 0.53 ± 0.04, and 0.57 ± 0.05 for *I*, *R* and *V* filters, respectively, before the break and $\alpha = 2.32 \pm 0.8$, 2.45 ± 0.4, and 2.26 ± 0.5 for *I*, *R* and *V* filters respectively after the break.

GRB 180618A is a short GRB with extended emission as discussed by Sakamoto et al. (2018). Our upper limits on polarization are large for *I* and *R* filters at a later time because the source is fainter and the noise is high as shown in Fig. 5. For the *V* filter the upper limit values are better constrained because of the higher signal-to-noise ratio in this filter for the source. For 30 min of stacked data we get polarization values of $<$ 5.26 per cent, $<$ 12.24 per cent, and $<$ 6.78 per cent and GISP values of 0.51 per cent, 0.58 per cent, and 0.63 per cent for *I*, *R*, and *V* bands, respectively. Further detailed analysis of GRB 180618A RINGO3 data will be presented by Jordana-Mitjans et al. (2022).

4.9 GRB 190114C

The LT observed this GRB ∼ 3 min after the burst time of 20:57:02.341 UTC and made observations using RINGO3 in *I*, *R*, and *V* bands. After the first 30 min of RINGO3 observations, IO:O was triggered and made observations in SDSS *r* band. Since the GRB was bright, more RINGO3 observations were taken after the IO:O observations. Detailed analysis of the LT follow-up observations and data from other telescopes has been presented in Jordana-Mitjans et al. (2020). Here we present a similar analysis to other GRBs. The light curve and power-law fit agree well with the results from Jordana-Mitjans et al. (2020) as seen in Fig. 3. The best fit for the RINGO3 light curve is a broken power law with a break at 401 s (we find the best fit to have the same break time for all the filters unlike in Jordana-Mitjans et al. 2020). We get $\alpha = 1.43 \pm 0.03$, 1.50 ± 0.02, and 1.47 ± 0.02 for *I*, *R*, and *V* filters, respectively, before the break and $\alpha = 0.87 \pm 0.02$, 0.94 ± 0.01, and 0.99 ± 0.02 for *I*, *R* and *V* filters, respectively, after the break. The jet break time is 0.21 d (Jordana-Mitjans et al. 2020).

Jordana-Mitjans et al. (2020) have presented detailed polarimetric analysis of GRB 190114C using RINGO3 data. Here we perform our polarimetric RINGO3 GRB analysis for 10 min stacked data. We obtain a polarization detection for the earlier time period and the polarization values are low; mostly coming from the ISP of the host galaxy as seen by Jordana-Mitjans et al. (2020). We note a slight difference in polarization measurements compared to Jordana-Mitjans et al. (2020) due to a difference in time intervals of our measurements and a different error calculation technique. For these data points we performed permutation analysis and found detections for a few points as presented in Table 7. There are two points in the *I* band for the time interval 803–1403 and 1403–2003 s and one data point in the *R* band for the time interval 803–1403 s whose error values do not cross the zero-point, however, their permutations ranks are lower than 0.95. Hence, we do not consider these values as detection and present them as the upper limit in Fig. 5. For 30 min of stacked data we get polarization values of $<$ 2.65 per cent, $<$ 2.78 per cent, and $<$ 2.21 per cent and GISP values of 0.07 per cent, 0.08 per cent, and 0.09 per cent for *I*, *R*, and *V* bands, respectively. Jordana-Mitjans et al. (2020) estimated the polarization contribution of the host galaxy to be $<$ 3.9 per cent, $<$ 4.5 per cent, and $<$ 4.5 per cent (larger than the detected polarization) therefore the detected polarization could easily be interpreted as simply coming from the dust in the host galaxy confirming our earlier work (Jordana-Mitjans et al. 2020).

4.10 GRB 191016A

There was a delay in LT observations of this GRB and initial IO:O observations were made in SDSS *r* band 40 min after the trigger time

of 04:09:00 UTC. We made RINGO3 follow-up observations 66 min after the trigger time in *I*, *R*, and *V* filter. Even though it was observed much later, the afterglow was bright enough to be detected in all the filters. Magnitude and flux calibrations were done with stars in the field and Galactic extinction of $A_V = 0.281, A_R = 0.222, A_I = 0.159$, $A_{r'} = 0.239$ was also corrected. The gamma-ray burst duration was inferred to be $T_{90} = 220 \pm 183$ s from *Swift* and the photometric redshift of the burst is 3.29 ± 0.40 (Smith et al. 2021).

Detailed analysis for the GRB is presented in Shrestha et al. (2022). Briefly, the light curve is best fitted by broken power law with different break point for different filters. For initial IO:O data the best-fitting model shows a simple power-law decay with decay index of 1.24. For RINGO3 *I*, *R*, and *V* bands the best-fitting models have decay index of 0.97 ± 0.07, 0.98 ± 0.07, and 1.25 ± 0.1 before the break time of 6146, 6087, and 5247 s. After the break the decay indices are 0.04 ± 0.17, -0.44 ± 0.17, and 0.01 ± 0.09, respectively. This plateau phase is also seen by Pereyra et al. (2022). The difference in decay indices during the plateau phase is hard to explain. One possibility presented by Shrestha et al. (2022) is the difference in electron energy distribution indexes in the blast wave and the reverse shock because the reverse shock is subrelativistic. Further analysis could be found in Shrestha et al. (2022). Shrestha et al. (2022) calculated the jet break time for this GRB to be 0.53 d with a limited number of data points. Later, Pereyra et al. (2022) calculated the jet break time using a larger number of data and found it to be between 0.24 to 0.52 d after the trigger. Using these two values along with *Swift* XRT data, we present 0.52 d as jet break time for this GRB.

We present results of bias-corrected polarization degree in Fig. 5. We get polarization detection at 1 sigma level in all three filters at different time period. One hour stacked data shows polarization values of < 3.83 per cent, < 5.23 per cent, and < 3.7 per cent, respectively. The GISP estimates for this GRB are 0.66 per cent, 0.75 per cent, and 0.8 per cent in *I*, *R*, and *V* bands, thus a very negligible contribution to our polarization measurements. We also calculated the ISP contribution of the host galaxy for this GRB. The best fit model from Smith et al. (2021) shows $A_V = 0.354$ for the host galaxy, and calculating the ISP using this extinction value for Milky Way-like dust gives 1.0 per cent, 1.1 per cent, and 1.2 per cent for *I*, *R*, and *V* bands. However, in Smith et al. (2021) the best-fitting model shows Small Magellanic Cloud (SMC)-like dust for the host galaxy and using SMC-like dust (Rodrigues et al. 1992) to estimate host galaxy ISP gives 0.92 per cent, 1.18 per cent, and 1.45 per cent for *I*, *R*, and *V* bands, respectively. Hence, the detected polarization is intrinsic polarization.

Our polarization result matches well with our previous analysis presented in Shrestha et al. (2022) which showed that the combination of polarimetry and photometry favours scenarios with energy injection from the central engine. In this case, slower magnetized ejecta from the central engine catches up with the decelerating blast wave and causes forward and reverse shocks. This short-lived reverse shock can explain the polarization detection we see near the plateau phase of the light curve.

5 DISCUSSIONS

We have presented polarimetric and photometric analysis of ten GRBs observed by RINGO3. Four of them, GRB 140430A, GRB 141214A, GRB 190114C, and GRB 191016A have been published separately in Kopač et al. (2015), Jordana-Mitjans et al. (2020, 2021), Shrestha et al. (2022), in this paper we have carried out a uniform re-reduction and analysis of the whole sample. Our analysis produces similar values of polarization degree and EVPA for these GRBs as previously noted in the published papers. We have presented light curves of GRB 130606A, 130610A, and 130612A which have been fit with a power law; we have presented the decay indices (α) for these GRBs for all the three RINGO3 wave bands except for GRB 130606A for which we only have good SNR for the *I* band as shown in Fig. 2. The XRT light curve for GRBs in the same time period is also presented. For all sources, other than GRB 140430A, we see the XRT light curve is similar to their optical light curves. Hence the X-ray photons in these events should originate from the forward shocks.

For most of the cases, the decay indices for the photometric light curve are less than 1.5 which shows we are observing the forward shock dominated light curve (Sari 1999; Kobayashi & Sari 2000; Zhang & Mészáros 2004; Gomboc et al. 2009; Japelj et al. 2014) in some cases with energy injection (decay indices can be closer to 0.5). However, for the case of GRB 130606A and GRB 180618A (after the break) we observed decay index values greater than 1.5. For GRB 130606A it could be the reverse shock dominated emission we are seeing but we do not have polarization degree calculations due to the instrument not being well calibrated. And for GRB 180618A, the steeper decay could be due to the jet break instead of a reverse shock emission. However, we note that the flattening in the X-ray at later times (alpha $= 1.04$ at $t > 5483$s) cannot be explained in a simple jet model. GRB 151215A and GRB 180325A have light curves which could be modelled by a single power law. Their decay indices are smaller than 1.5; suggesting that the forward shock emission is dominating or suggestive of some energy injection. For these cases, we get polarization upper limits in three wavelengths, which is expected in the case of forward shock dominated emission (Rossi et al. 2004). Thus, it is possible that most of the observed polarization is contributed by dust in the host galaxy. GRB 180618A is a short GRB with extended emission. The light curve of this GRB is best fit by a broken power law with a break at 1370 s. Initially the light curve showed a shallow decay of 0.48, 0.53, and 0.57 for *I*, *R*, and *V* band, respectively. After the break the decay is sharper with 2.32, 2.45, and 2.26 for *I*, *R*, and *V* band, respectively. There are few points after the break, thus the sharp decay is not well modelled. We do not detect any polarization and get upper limits in polarization. Further discussion on GRB 180618A will be presented in Jordana-Mitjans et al. (2022).

There are few polarization observations of GRB early afterglows in the literature. Uehara et al. (2012) detected polarization in the early afterglow of GRB 091208B and King et al. (2014) reported early-time polarization of GRB 131030A. We investigated the relationship between the polarization signal and various properties of GRBs such as decay index in Fig. 6, isotropic energy $E_{\rm iso}$, peak energy E_p, BAT peak, T_{90}, redshift, and extinction of the Milky Way as shown in Fig. 7. In addition, we also checked the relation between polarization and temporal distance of jet break from our observation. As most of the data points are upper limits, we performed survival analysis (Feigelson & Nelson 1985) using the PYTHON package LIFELINES (Davidson-Pilon et al. 2020) to check for any co-relation between polarization signal and different GRB parameters as noted. For all of the cases we get a concordance index close to 0.5, which is the expected results from random predictions, hence, we cannot conclude any relation from our data set. In order to get a better relation between polarization and various properties we need to increase the number of observations of GRB early afterglows. The increased sensitivity of the new polarimeter MOPTOP (Shrestha et al. 2020) on the LT will improve the number of polarization observations of early afterglows in the future.

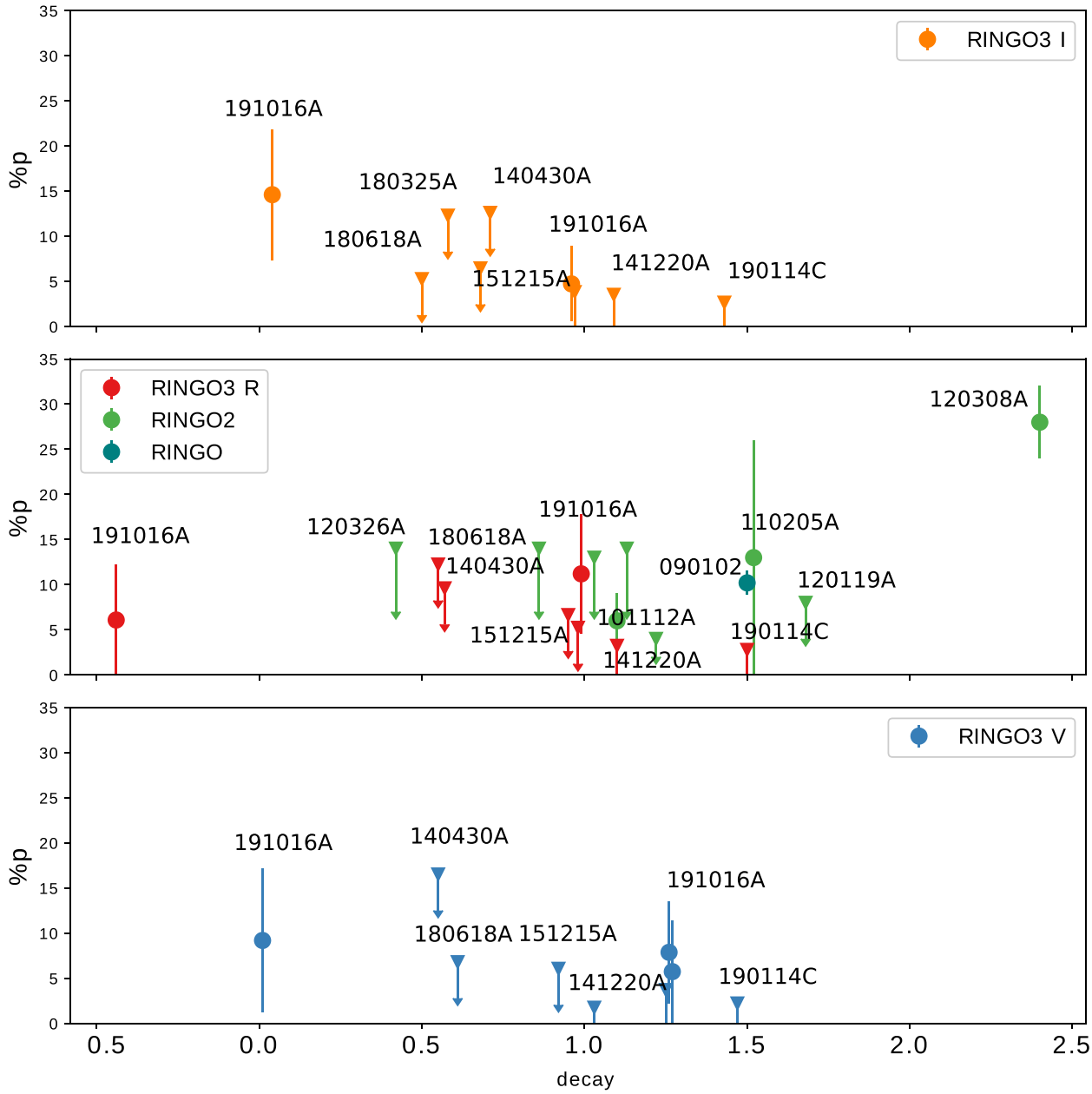

Figure 6. Observed polarization values (all observed data stacked for upper limit along with detected polarization values) with respect to the decay indices deduced from the light curves. Three panels show results for *I*, *R*, and *V* band results from top to bottom, respectively. For *R* band, we also present results from RINGO2 observations previously presented in Steele et al. (2017). Names of the GRBs are given for all the cases except for GRB 100805A, GRB 110726A, GRB 120311A, and GRB 120327A from RINGO2 observations for better visibility of points in the plot. Polarized detection is presented as a circle and upper limit is presented as a inverted triangle. For GRB 191016A, we present all the detected polarization for the different time periods and the decay index value of the corresponding time period is plotted.

5.1 Polarization and decay index

In the literature, we find most of the high degree of polarization values to be observed for the case of reverse-shock emission (Steele et al. 2009; Mundell et al. 2013). When the GRB jet interacts with the local ambient medium, there are forward and reverse shock components: the reverse shock is short lived emission and decays faster than the forward shock emission. The decay index for the light curves where reverse shock is dominating is expected to be greater than 1.5 (Sari 1999; Kobayashi & Sari 2000; Zhang & Mészáros 2004; Gomboc et al. 2009; Japelj et al. 2014). Previously, Steele et al. (2017) presented how polarization varies with decay index for nine different GRBs observed when RINGO2 was online (see fig. 13 in their paper). Here we add to this data set and study how polarization changes with decay index for *I*, *R*, and *V* bands in Fig. 6 top, middle, and bottom panels, respectively. In the middle panel, we also include results from RINGO2 observations as presented in Steele et al. (2017). All the upper limits presented here are for stacked data shown in Tables 6 and 7 and B 190114C and GRB 191016A detected polarization is also

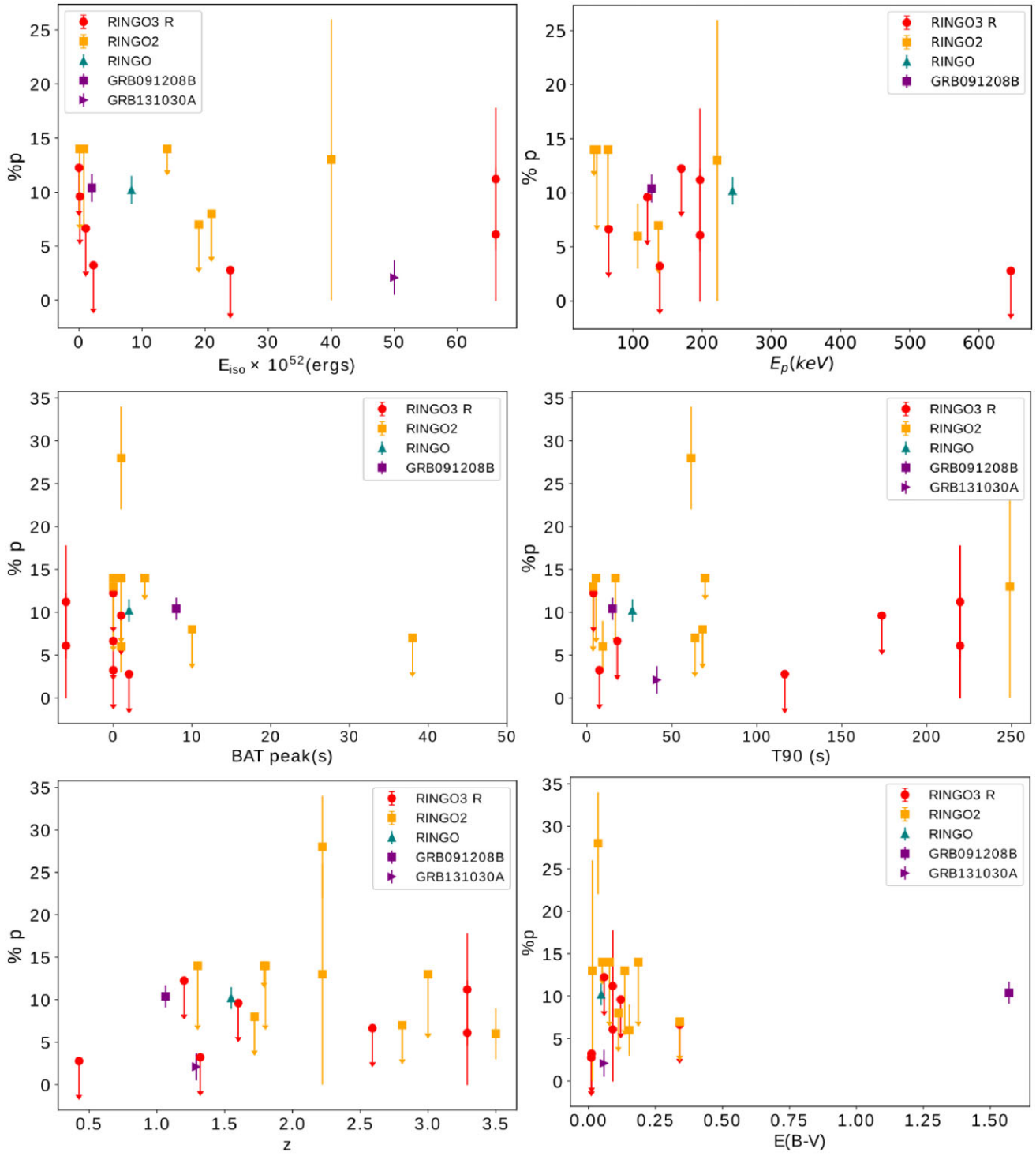

Figure 7. Observed polarization values (stacked) from RINGO3 along with all the early time optical afterglow polarization observations in the literature with respect to different GRB properties. Upper limit are presented as downward arrow. Polarization values for RINGO2 are from Steele et al. (2017), for RINGO are from Steele et al. (2009), GRB 091208B is from Uehara et al. (2012), and GRB 131030A is from King et al. (2014).

presented. For GRB 191016A, polarization has been detected before the break in light curve and after the break which is also plotted in Fig. 6. In the RINGO3 data set we do not find any cases with a decay index close to 2, thus we suggest that our observed cases are for forward shock dominated emission, which is not highly polarized as shown in Fig. 6. To get a better relation between polarization and decay index we need to increase the number of observations of GRB early afterglows, where the reverse shock is dominated which will be possible thanks to new polarimeter MOPTOP (Shrestha et al. 2020) on the LT.

6 CONCLUSIONS

We have presented photometric and polarimetric results and analysis of ten GRBs out of 67 GRBs triggered by RINGO3 during the time period of 2013 to 2020. For the first three GRBs, instrument polarization was not well constrained so we only present photometry results. For the subsequent seven GRBs we present both photometric and polarimetric results with polarization degree (or upper limits) and EVPA values in the case of detection. Out of these GRBs, polarization was detected for GRB 190114C and GRB 191016A. Further analysis of GRB 190114C showed that detected polarization was contributed by the host galaxy dust. For GRB 191016A the contribution from the host galaxy, assuming SMC-like dust, is negligible and thus the detected polarization is considered to be intrinsic.

We created light curves of all ten GRBs using RINGO3 for *I*, *R*, and *V* band (where available), IO:O r' band and RATCam r' band data. We performed best fits for these RINGO3 light curve using either single power law or broken power law and report the decay indices for these light curves. We analysed the relation between decay index and polarization degree, since we mostly observed slowly decaying events we cannot provide clear correlation between decay index and polarization degree. We performed survival analysis to investigate if there is any co-relation between decay index and polarization. From our survival analysis we get concordance index of 0.47 which shows that with our limited data, we do not see any co-relation. Hence, we need more early time observations of GRB events to study the relation between polarization and decay index.

We make an intrinsic detection of polarization for GRB 191016A which has a late peak of at least 1000 s after the BAT trigger (Smith et al. 2021). The source is bright enough to perform polarimetry and photometry even 66 min after the BAT trigger. The light curve is best fitted by a broken power law at 5500 s after the BAT trigger and we get a shallow decay index close to 1 for all three wavelengths before the break time and it plateaus after the break time. With a high level of detected polarization ($>$ 9 per cent) and no jet-break like feature, we deduce that the light curve has reverse shock emission and the shallow decay is due to the energy injection to the forward shock/blast wave.

The GRB 190114C case shows that even a detection of low polarization degree can help us understand the afterglow emission mechanism. For the GRB 191016A case, polarization and EVPA calculations along with the light curve allowed us to carry out detailed analysis of the afterglow emission. In the absence of polarization analysis, the GRB 191016A afterglow would have been considered as forward shock emission. However, polarization and EVPA measurements point towards the possibility of reverse shock emission in the afterglow. Thus, polarization observations of GRBs can provide crucial clues to getting detailed information about the event along with photometric and spectroscopic observations.

RINGO3 polarimeter have successfully observed various early optical afterglows of GRBs within few hundred seconds of trigger. The results presented in this paper shows the importance of simultaneous multicolour photometry and polarimetry (colours$>$2) which helps us to determine the underlying emission mechanism. New polarimeters with increased sensitivity to probe a larger statistical sample over a significant time period of their evolving emission would open new windows on GRB physics.

ACKNOWLEDGEMENTS

Operation of LT on the island of La Palma by Liverpool John Moores University at the Spanish Observatorio del Roque de los Muchachos of the Instituto de Astrofisica de Canarias is financially supported by the UK Science and Technologies Facilities Council (STFC). Financial support for the development of MOPTOP was provided by the STFC PRD scheme. MS is supported by an STFC consolidated grant number (ST/R000484/1) to LJMU. We acknowledge with thanks the variable star observations from the AAVSO International Database contributed by observers worldwide and used in this research. This research made use of PHOTUTILS, an Astropy package for detection and photometry of astronomical sources (Bradley et al. 2019). AG acknowledges the financial support from the Slovenian Research Agency (research core funding P1-0031, infrastructure program I0-0033, project grants J1-8136, J1-2460) and networking support by the COST Actions CA16104 GWverse and CA16214 PHAROS. CGM and NJM thank Hiroko and Jim Sherwin for financial support. This work made use of data supplied by the UK Swift Science Data Centre at the University of Leicester. We would like to thank our anonymous referee for thorough and thoughtful comments that have greatly improved the paper.

DATA AVAILABILITY

All the observational data are freely available online in the LT archive at https://telescope.livjm.ac.uk/.

REFERENCES

Arnold D. M., Steele I. A., Bates S. D., Mottram C. J., Smith R. J., 2012, in McLean I. S., Ramsay S. K., Takami H., eds, Proc. SPIE Conf. Ser. Vol. 8446, Ground-based and Airborne Instrumentation for Astronomy IV. SPIE, Bellingham, p. 84462J
Arnold D., 2017, PhD thesis, Liverpool John Moores University, Liverpool
Bessell M. S., Castelli F., Plez B., 1998, A&A, 333, 231
Bradley L. et al., 2019, astropy/photutils: v0.6. Available at: https://doi.org/10.5281/zenodo.2533376
Castro-Tirado A. J. et al., 2013, GCN Circ., 14796, 1
Clarke D., Neumayer D., 2002, A&A, 383, 360
Covino S., Gotz D., 2016, Astron. Astrophys. Trans., 29, 205
Cummings J. R. et al., 2013, GCN Circ., 14842, 1
Cummings J. R., D'Elia V., Gehrels N., Lien A. Y., Palmer D. M., Sbarufatti B., Siegel M. H., 2014, GCN Circ., 17196, 1
Davidson-Pilon C. et al., 2020, CamDavidsonPilon/lifelines: v0.23.9, Zenodo. Available at: 10.5281/zenodo.3629409
de Ugarte Postigo A., Thoene C. C., Gorosabel J., Tanvir N., Fynbo J. P. U., Pesev P., Gomez Velarde G., Perez Valladares D., 2014, GCN Circ., 17198, 1
Evans P. A. et al., 2009, MNRAS, 397, 1177
Feigelson E. D., Nelson P. I., 1985, ApJ, 293, 192
Ghisellini G., Lazzati D., 1999, MNRAS, 309, L7
Gibson S. L., Kennea J. A., Page K. L., Palmer D. M., Sbarufatti B., Siegel M. H., 2015, GCN Circ., 18691, 1
Gomboc A. et al., 2009, in Meegan C., Kouveliotou C., Gehrels N., eds, AIP Conf. Proc. Vol. 1133, Gamma-ray Burst: Sixth Huntsville Symposium. Am. Inst. Phys., New York, p. 145
Gropp J. D. et al., 2019a, GCN Circ., 23688, 1
Gropp J. D., Klingler N. J., Lien A. Y., Moss M. J., Palmer D. M., Sbarufatti B., Neil Gehrels Swift Observatory Team, 2019b, GCN Circ., 26008, 1
Guidorzi C. et al., 2006, PASP, 118, 288
Hamburg R., Bissaldi E., Fermi GBM Team, 2018, GCN Circ., 22794, 1
Hamburg R., Veres P., Meegan C., Burns E., Connaughton V., Goldstein A., Kocevski D., Roberts O. J., 2019, GCN Circ., 23707, 1
Heintz K. E., Fynbo J. P. U., Malesani D., 2018, GCN Circ., 22535, 1
Japelj J. et al., 2014, ApJ, 785, 84
Jermak H. et al., 2016, MNRAS, 462, 4267
Jermak H., 2017, PhD thesis. Liverpool John Moores University, Liverpool
Jordana-Mitjans N. et al., 2020, ApJ, 892, 97

Jordana-Mitjans N. et al., 2021, MNRAS, 505, 2662
Jordana-Mitjans N. et al., 2022, submitted
King O. G. et al., 2014, MNRAS, 445, L114
Kobayashi S., 2019, Magnetic Fields in Gamma-Ray Bursts and Their Polarised Emission. Springer International Publishing, Cham, p. 337
Kobayashi S., Sari R., 2000, ApJ, 542, 819
Kopač D. et al., 2015, ApJ, 813, 1
Kruehler T., Malesani D., de Ugarte Postigo A., Melandri A., Fynbo J. P. U., 2014, GCN Circ., 16194, 1
LaPorte S. J. et al., 2018, GCN Circ., 22790, 1
Lazzati D., 2006, New J. Phys., 8, 131
Lien A. et al., 2016, ApJ, 829, 7
Metzger B. D., Giannios D., Thompson T. A., Bucciantini N., Quataert E., 2011, MNRAS, 413, 2031
Monet D. G. et al., 2003, AJ, 125, 984
Mundell C. G. et al., 2013, Nature, 504, 119
Pereyra M. et al., 2022, MNRAS, 511, 6205
Piran T., 1999, Phys. Rep., 314, 575
Plaszczynski S., Montier L., Levrier F., Tristram M., 2014, MNRAS, 439, 4048
Racusin J. L. et al., 2013, GCN Circ., 14874, 1
Rodrigues C., Magalhaes A. M., Coyne G., Piirola V., 1992, in Singh P. D., ed., Proc. IAU Symp. 150, Astrochemistry of Cosmic Phenomena. Springer, Berlin, p. 109
Rossi E. M., Lazzati D., Salmonson J. D., Ghisellini G., 2004, MNRAS, 354, 86
Sakamoto T. et al., 2018, GCN Circ., 22796, 1
Sari R., 1999, ApJ, 524, L43
Schlafly E. F., Finkbeiner D. P., 2011, ApJ, 737, 103
Selsing J., Fynbo J. P. U., Heintz K. E., Watson D., 2019, GCN Circ., 23695, 1
Serkowski K., Mathewson D. S., Ford V. L., 1975, ApJ, 196, 261
Shrestha M. et al., 2022, MNRAS, 509, 5964
Shrestha M., Steele I. A., Piascik A. S., Jermak H., Smith R. J., Copperwheat C. M., 2020, MNRAS, 494, 4676
Siegel M. H. et al., 2014, GCN Circ., 16190, 1
Siegel M. H., LaPorte S. J., Swift/UVOT Team, 2018, GCN Circ., 22810, 1
Smette A., Ledoux C., Vreeswijk P., De Cia A., Petitjean P., Fynbo J., Malesani D., Fox A., 2013, GCN Circ., 14848, 1
Smith K. L. et al., 2021, ApJ, 911, 43
Steele I. A. et al., 2004, in Oschmann J. M., Jr, ed., Proc. SPIE Conf. Ser. Vol. 5489, Ground-based Telescopes. SPIE, Bellingham, p. 679
Steele I. A. et al., 2017, ApJ, 843, 143
Steele I. A., 2001, Astron. Nachr., 322, 307
Steele I. A., Mundell C. G., Smith R. J., Kobayashi S., Guidorzi C., 2009, Nature, 462, 767
Tanvir N. R., Wiersema K., Xu D., Fynbo J. P. U., 2013, GCN Circ., 14882, 1
Toma K., 2013, preprint (arXiv:1308.5733)
Troja E. et al., 2018, GCN Circ., 22532, 1
Troja E., Piro L., Vasileiou V., Omodei N., Burgess J. M., Cutini S., Connaughton V., McEnery J. E., 2015, ApJ, 803, 10
Uehara T. et al., 2012, ApJ, 752, L6
Ukwatta T. N. et al., 2013, GCN Circ., 14781, 1
Wilking B. A., Lebofsky M. J., Rieke G. H., 1982, AJ, 87, 695
Xu D., Tanvir N. R., Malesani D., Fynbo J. P. U., Jakobsson P., Saario J., 2015, GCN Circ., 18696, 1
Yasuda T., Urata Y., Enomoto J., Tashiro M. S., 2017, MNRAS, 466, 4558
Zhang B., Fan Y. Z., Dyks J., Kobayashi S., Mészáros P., Burrows D. N., Nousek J. A., Gehrels N., 2006, ApJ, 642, 354
Zhang B., Mészáros P., 2004, Int. J. Mod. Phys. A, 19, 2385

SUPPORTING INFORMATION

Supplementary data are available at *MNRAS* online.

RINGO3_GRBs

Please note: Oxford University Press is not responsible for the content or functionality of any supporting materials supplied by the authors. Any queries (other than missing material) should be directed to the corresponding author for the article.

This paper has been typeset from a TEX/LATEX file prepared by the author.